JACS
JOURNAL OF THE AMERICAN CHEMICAL SOCIETY

ARTICLE

pubs.acs.org/JACS

How Do Aminoadamantanes Block the Influenza M2 Channel, and How Does Resistance Develop?

Hadas Leonov,[†,‡] Peleg Astrahan,[†] Miriam Krugliak, and Isaiah T. Arkin*

Department of Biological Chemistry, The Alexander Silberman Institute of Life Sciences, The Hebrew University of Jerusalem, Edmund J. Safra Campus, Jerusalem 91904, Israel

Supporting Information

ABSTRACT: The interactions between channels and their cognate blockers are at the heart of numerous biomedical phenomena. Herein, we unravel one particularly important example bearing direct pharmaceutical relevance: the blockage mechanism of the influenza M2 channel by the anti-flu amino-adamantyls (amantadine and rimantadine) and how the channel and, consequently, the virus develop resistance against them. Using both computational analyses and experimental verification, we find that amino-adamantyls inhibit M2's H^+ channel activity by electrostatic hindrance due to their positively charged amino group. In contrast, the hydrophobic adamantyl moiety on its own does not impact conductivity. Additionally, we were able to uncover how mutations in M2 are capable of retaining drug binding on the one hand yet rendering the protein and the mutated virus resistant to amino-adamantyls on the other hand. We show that the mutated, drug-resistant protein has a larger binding pocket for the drug. Hence, despite binding the channel, the drug remains sufficiently mobile so as not to exert a H^+-blocking positive electrostatic hindrance. Such insight into the blocking mechanism of amino-adamantyls, and resistance thereof, may aid in the design of next-generation anti-flu agents.

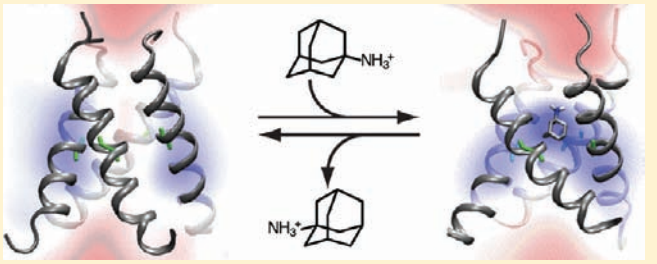

INTRODUCTION

M2 is a homotetrameric, 96-residue bitopic protein in the membrane of the influenza A virus. It forms a selective H^+ channel that is critical for the infectivity of the influenza virus, as it plays a key role in the virus's entry process.[1,2] The virus enters the host cell via endocytotic uptake,[3] and upon endosome acidification, two processes ensue: viral membrane fusion and opening of the M2 channel, which results in a H^+ influx into the virus interior.[4] Acidification of the viral lumen triggers the uncoating of the viral RNA into the host cell.

M2 is composed of an extracellular N-terminal domain of 24 residues, a 19-residue transmembrane (TM) region, and a C-terminal cytoplasmic domain of 54 residues. The TM region forms a homotetrameric helical bundle[5−10] that acts as a slow H^+ channel.[1,2,11,12] Experimental and computational studies have attributed the activation of the channel to the H37 residues in the TM region, where protonation is thought to open the channel.[4,13−17]

Interest in the M2 channel arises from the fact that its H^+ channel activity can be inhibited by the amino-adamantyls, such as amantadine (1-aminoadamantane) and rimantadine (1-(1-adamantyl)ethylamine), two commercial drugs that terminate the replication of influenza A[18,19] (see Supporting Information, supplementary Figure 1). Over the past decades however, mutations have enabled the virus to develop resistance to amino-adamantyls in over 90% of current influenza A strains.[20] A genetic analysis of amantadine-resistant and amantadine-sensitive strains indicated that the mutations that conferred amantadine resistance were localized to four amino acids in the TM domain of M2: V27, A30, S31, and G34.[18,21]

A study measuring the direct binding of amantadine to the M2 channel revealed that mutations at positions 30 and 31 cause the channel to lose the ability to bind the drug, while mutations at position 27 maintain drug binding.[22] The difference between the mutations and their effect was then explained by the type of mutation that occurred: the mutations at positions 30 and 31 were to larger and more polar amino acids (A30T, S31N), whereas the amino acid at position 27 was replaced by a smaller counterpart (V27A, I27S, I27T).

Since amantadine was found to act on the M2 channel, numerous studies have been undertaken to elucidate how and where it binds. Among the first studies in the field were MD simulations of the M2 helical bundle model[23,24] and neutron diffraction studies.[25] Both studies suggested that amantadine is placed in the pore between residues V27 and S31. In 2007, a structural model of M2 in the presence of amantadine was determined by solid-state NMR spectroscopy,[26] and later simulations were conducted to model amantadine onto that structure.[27] Residues A30 and S31 were observed to interact principally with the inhibitor, whereas occasional interactions occurred with V27, I33, and G34. Amantadine was found to be

Received: March 27, 2011
Published: May 02, 2011

oriented in the channel such that its amine group was pointing to the C-terminal side ("amine-down").

In the following year, an X-ray study determined the structure of the M2 TM domain (S22−L46) with and without amantadine.[28] The amantadine-bound protein was a mutant form of M2 (G34A) that was crystallized at pH 5.3. The X-ray structure (3.5 Å resolution) presented an electron density that appeared only in the presence of amantadine, surrounded by residues 27, 30, 31, and 34. At the same time, a solution NMR study of a longer M2 peptide (S23−K60) in the presence of rimantadine advocated a different binding location, where rimantadine binds the outer rim of the helical bundle, interacting with residues 40−45.[29] Computational solvent mapping of amantadine in these two structures had found the largest hotspot at the internal binding site of the channel, interacting with a subset of the residues 27, 30, 31, and 34, while the amine is pointing at the N-terminal direction ("amine-up"). Further docking and energy considerations illustrated a second binding spot outside the channel in the C-terminal region.[30]

A solid-state NMR study from 2009 examined the chemical shifts perturbations with and without amantadine and once again reinforced the observations of the internal binding site near the N-terminal TM region. In addition, it suggested an amine-up orientation, since only then is a hydrogen bond with S31 possible.[31] A subsequent solid-state NMR study revealed a lower affinity binding site at the C-terminus, which is employed when the amantadine:M2 ratio is increased so that the internal binding site is saturated.[32] Understanding the interactions between the current, known drugs and the channel may enhance our ability to design the next generation of M2 blockers that might serve as effective anti-flu agents.

Herein, we attempt to characterize the binding site and interactions of amino-adamantyl inhibitors in the channel, unravel the mechanism that enables the inhibition of conductivity, and finally, understand how mutations confer drug resistance. We employ a computational route that leads to predictions we could verify experimentally. In these ways, we provide a detailed picture of the mechanism of amino-adamantyl inhibition and resistance thereof.

RESULTS AND DISCUSSION

Our goal was to understand the mechanism by which amino-adamantyls inhibit the M2 channel at the molecular level, using both computational and experimental analyses. We therefore started by performing calculations aimed at identifying the binding site of various amino-adamantyl derivatives.

A simulation system was constructed to investigate the M2 TM tetrameric complex in a hydrated lipid bilayer by molecular dynamics (MD) simulations. The simulation system was equilibrated for 20 ns, as evident from the stabilization of the structures (Supporting Information, supplementary Figure 2). Subsequently, a representative structure of the equilibrated stage was taken for further analyses.

Drug Binding Location. We next proceeded to calculate the energetics of drug binding to the channel pore using a potential of mean force (PMF) analysis. In brief, the PMF is defined as the change in free energy as a function of a particular reaction coordinate. Since the membrane plane coincided with the *xy* plane of the simulation system, the reaction coordinate was simply the movement of the drug along the *z* axis through the channel. The umbrella sampling approach[33] and the standard weighted histogram analysis method (WHAM)[34] were employed, facilitating sufficient sampling in thermodynamically unfavorable regions.

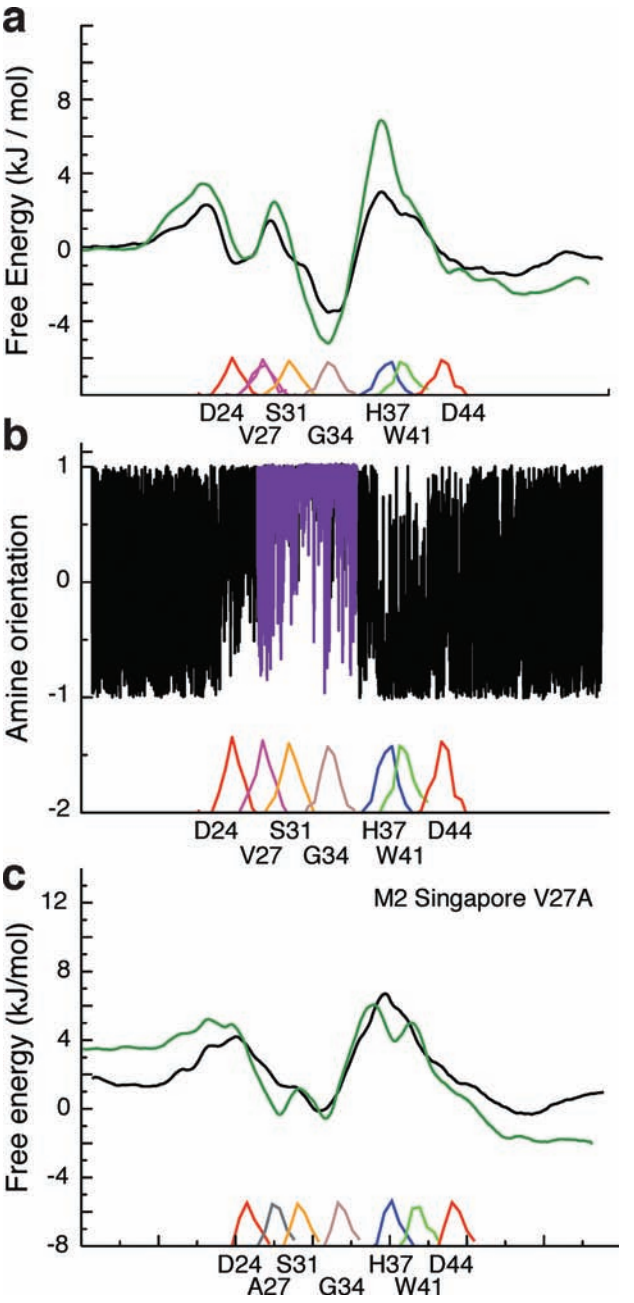

Figure 1. (a) PMF profiles for amantadine (black) and rimantadine (green) along the M2 Singapore wild-type pore axis. (b) Amantadine's carbon-NH_3^+ vector orientation as a function of the reaction coordinate. A value of +1 indicates it points upward, and a value of −1 indicates a downward orientation. An expansion of the sampling time from 1 to 10 ns per simulation slab for the restricted pore region is shown in violet. For both plots the histograms represent the density distribution of pore-lining residues. (c) Same as (a) but for the V27A-resistant mutant.

The results of the PMF analysis for amantadine and rimantadine binding to the wild-type channel are shown in Figure 1a. It can be seen that the PMF curves for both inhibitors are similar, exhibiting three energy maxima, the largest (4−7 kJ/mol) at

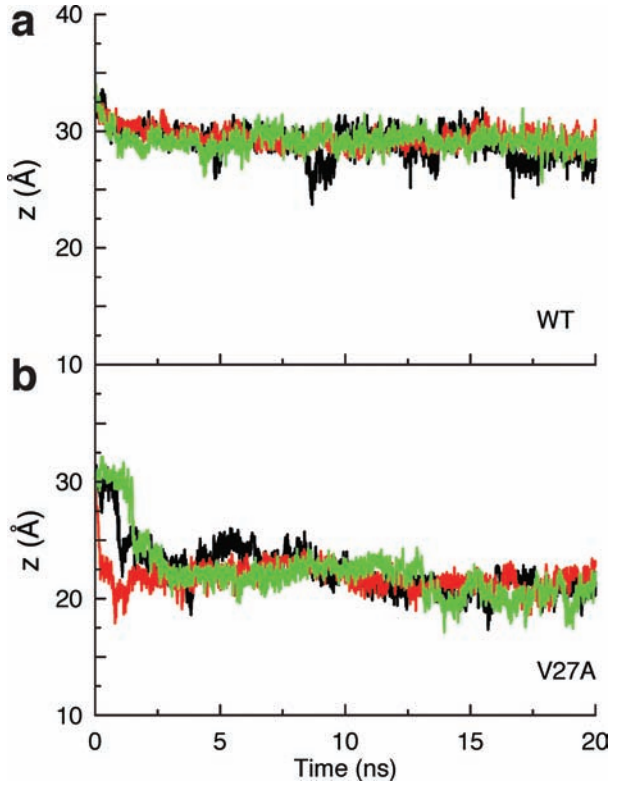

Figure 2. Movement of amantadine's center of mass on the *z*-axis (pore axis) during three independent trials of an unrestricted MD simulation. The simulations were performed for the wild-type (a) and V27A (b) strains. Each color represents an independent trial.

H37. The energy barrier at the histidines is expected, as both of the inhibitors and three of the histidines are positively charged in the simulation, thereby emulating a channel at pH < 6, which is most probably open.[35] However, the most significant observation is the local energy minimum that lies in the region between G34 and S31. The location of the energy trough is similar to that found in the X-ray structure,[28] and as such, henceforth we shall use it as the drug binding site. Finally, we note that the deeper energy trough of rimantadine in comparison to amantadine (Figure 1a) correlates qualitatively to the relative affinities of the two drugs. Specifically, rimantadine binds the channel more than an order of magnitude tighter than amantadine;[36] hence, one would expect a lower energy at the binding site in the PMF profiles, as we observe.

Drug Orientation in the Channel. We next proceeded to examine the orientation of the drug as a function of its position along the channel. Specifically, we focused on the location of the amine group of amantadine relative to the drug's center of mass. An orientation in which the amine group is facing the N-terminal of the pore (amine-up) was marked by a positive value of +1. The opposite amine-down orientation, in which the amine faces the C-terminal, is marked by a negative value of −1.

The data shown in Figure 1b indicate that the amantadine can freely rotate to any orientation regardless of the initial position when it is in bulk water. However, once it approaches the protein, it becomes more restrained, particularly between residues S22 and H37. Amantadine can still rotate to the opposite orientation, but it does so at a much lower frequency (see expansion of the sampling from 1 to 10 ns in Figure 1b). Eventually, amantadine is substantially restrained to the amine-up orientation between V27 and G34. It becomes looser once it reaches a wider region in the pore at G34 and H37. It is worth noting that, whereas amantadine preferred the amine-up orientation from the N-terminus to H37, beyond that point an amine-down orientation is assumed more frequently so that the charged amine is located as far as possible from the charged histidines once more. After amantadine exits the protein back into the solvent, it freely flips back and forth.

Calculations Predict an Electrostatic Inhibition Mechanism. As the PMF analysis predicted a preferred binding site of the drugs that coincided well with the X-ray results,[28] we could proceed to further examine the interactions between the inhibitors and the channel. Toward this end, we ran longer, unrestrained simulations of the channel with amantadine initially positioned in the binding site. Subsequently we could analyze detailed properties of the system in hopes of uncovering the inhibition mechanism of the drug.

Initially we examined the movement of the drug relative to its starting position. Specifically, the *z*-coordinate movements of amantadine's center of mass were examined as a function of the simulation time (Figure 2a). It can be seen that amantadine moved by 1−2 Å on the *z*-axis in the N-terminal direction and stabilized at that point. Even when random motions led the drug to move farther away, it returned to the same pore region at $z \approx 30$ Å. During the simulations, we have observed the formation of a water wire throughout the channel at several instances, thereby raising the question: How does amantadine inhibit the channel if not by a physical block?

With the stable structure of the channel-inhibitor complex at hand, we turned to examine the electrostatic potential in the region of the channel. Comparison of the electrostatic potentials of the apo-channel (Figure 3a) to an amantadine-bound channel (Figure 3b) clearly points to a positive potential centered above G34 arising from the charged amine of the amantadine. As control, the electrostatic potential was calculated for a channel bound to a neutral amantadine, and it was observed that the positive electrostatic potential does not exist in this instance (Figure 3c).

Taken together, our calculations allow us to hypothesize that amantadine inhibits the M2 channel via its positive charge, forming a prohibitive electrostatic potential for protons to transverse. Therefore, we proceeded to conduct experiments to test the validity of our hypothesis.

Experimental Proof of the Electrostatic Inhibition Mechanism. In order to experimentally examine the activity of the M2 channel and its inhibitors, we made use of a recently devised cell-based assay.[36] In brief, the assay monitors the growth retardation of bacteria due to the expression of the M2 channel in their periplasmic membrane. Consequently, any drug that blocks the channel will result in growth enhancement that can readily be measured. The method is sensitive and highly accurate, so as to enable detailed affinity measurements between the channel and its cognate blockers.[36]

Since our hypothesis posits that the charged amine in amantadine is responsible for channel blockage, it follows that its neutralization at elevated pH would result in loss of the drug's blocking activity. Therefore, we performed the M2 cell-based assay in a range of pH conditions (5.5−9.0) to examine the activity of amantadine and rimantadine as a function of pH.

The results in Figure 4a show that bacterial growth is drastically hampered by the expression of M2 throughout the entire pH range. In fact, the activity of M2 seems to increase

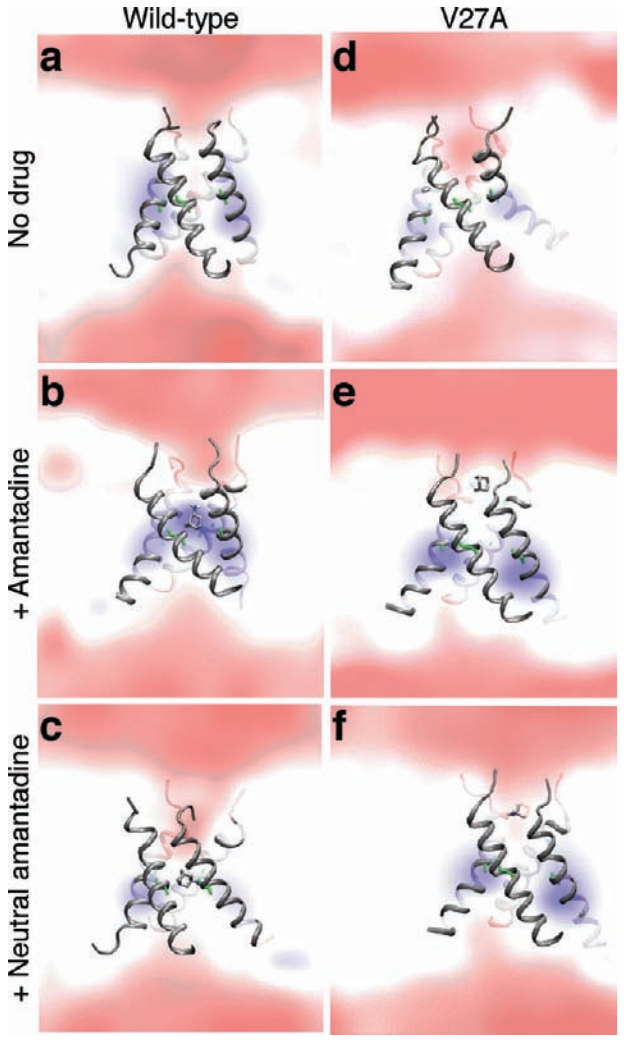

Figure 3. Time-averaged electrostatic potential of the M2 Singapore wild-type channel (a−c) and V27A mutant (d−f): (a,d) channel only; (b,e) channel with a charged amantadine; and (c,f) channel with a neutral amantadine. Blue and red represent positive and negative potential, respectively.

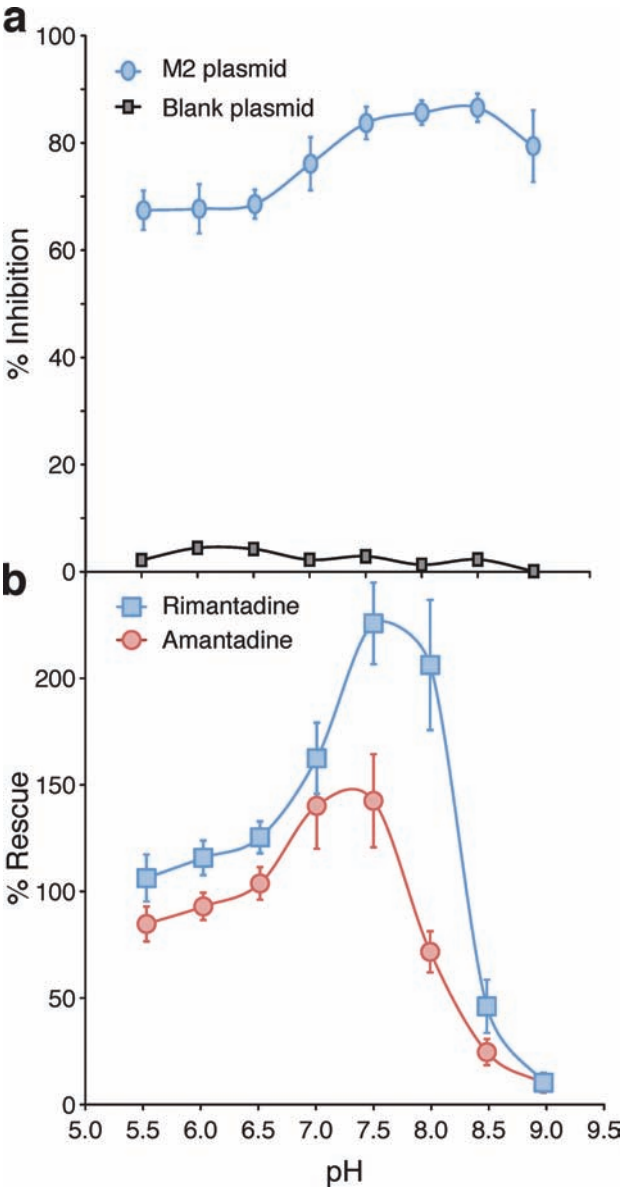

Figure 4. M2 activity and blockage at different pH conditions. (a) Percentage of bacterial growth inhibition ($n = 4$) when M2 is expressed (blue). For control (black), inhibition percentages are presented for cells lacking the M2 expression plasmid. IPTG was added to both bacterial cultures at equal concentration (40 μM), and the respective percentages were calculated relative to bacteria in which the IPTG was not added. (b) Growth rescue (i.e., drug activity) percentage ($n = 3$) for amantadine and rimantadine (both at 100 μM). The rescue percentages are calculated relative to growth conditions where no drug was added. In both panels the error bars represent the standard error of the mean, and n is the number of independent trials. The growth temperature was 28 °C.

somewhat as the pH is elevated, perhaps due to the fact that, when protons are scarce, a proton leakage is particularly deleterious. In other words, at elevated pH, bacterial growth rate might be limited due to difficulty in maintaining an appreciable protonmotive force when the concentration of protons is very low. Thus, any proton leakage might be particularly detrimental under basic conditions.

In stark contrast, the ability of amantadine and rimantadine to relieve growth retardation is dramatically dependent on pH. Specifically, the results depicted in Figure 4b indicate that amantadine loses its activity from pH 8.0 and upward, whereas rimantadine only becomes ineffective at pH 8.5 and above.

Hence, the experimental results are entirely consistent with our electrostatic blockage hypothesis, in that an increase in pH renders both drugs incapable of blocking the channel. This is what we predict should happen when the amine group deprotonates at increased pH, since a neutral amine cannot generate a local positive potential. Furthermore, the difference between the pH profiles of rimantadine and amantadine may provide further support to our hypothesis. While the exact pK_a values of amantadine or rimantadine when bound to the protein are not known, the known higher pK_a of rimantadine relative to amantadine in solution[37−39] is reflected in the higher pH at which rimantadine loses activity relative to amantadine: rimantadine is close to peak activity at pH 8, whereas at the same pH amantadine has lost more than 50% of its activity (see Figure 4b).

The results of the pH profile analyses of drug activity described above are consistent with our electrostatic blockage hypothesis, yet they are not entirely conclusive. For example, several other

dx.doi.org/10.1021/ja202288m |*J. Am. Chem. Soc.* 2011, 133, 9903–9911

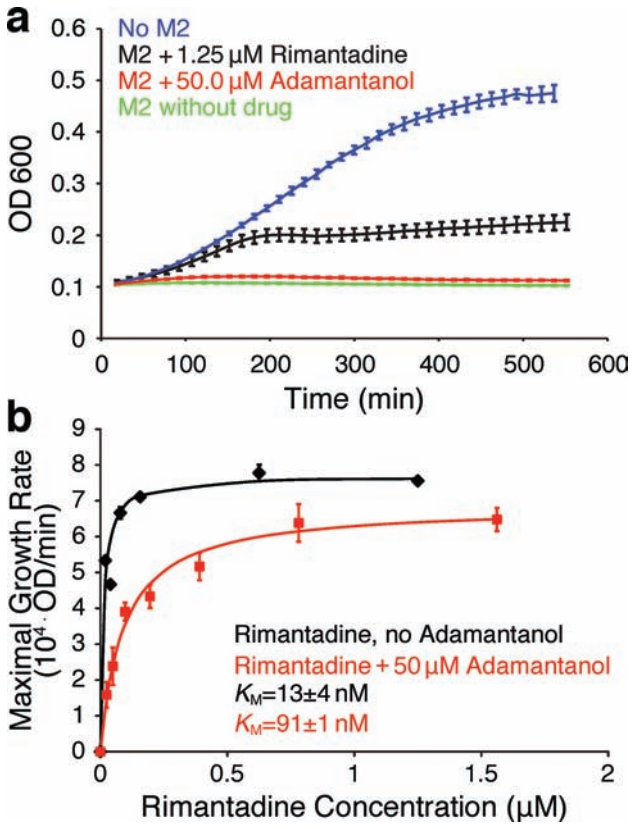

Figure 5. Activity of adamantanol. (a) Growth curves ($n = 8$) of bacteria expressing the M2 channel in the presence of 1.25 μM rimantadine (black) or 50 μM adamantanol (red). Bacteria that do not express the M2 channel (blue) and bacteria that express the channel without any drug (green) are used as control. (b) Competition analysis between adamantanol and rimantadine. The maximal growth rate of bacteria that express the M2 channel was monitored ($n = 8$) as a function of varying concentrations of rimantadine (black). Subsequently, the effect of 50 μM adamantanol on the ability of rimantadine to rescue the bacteria was measured to evaluate the competitive interaction between the two drugs (red). The resulting K_M values of rimantadine's activity are indicated in the graph. The lines indicate a least-squares nonlinear fit of the data to the standard Monod equation. In both panels the error represents the standard deviation, and n is the number of independent trials. The growth temperature was 30 °C, and the final IPTG concentration was 60 μM.

factors in the growth retardation analysis might be pH dependent, not the least of which is the activity of M2.[1] Therefore, we decided to perform an additional experimental analysis to prove our electrostatic blockage hypothesis. Specifically, we made use of an amantadine derivative that is neutral in the experimental conditions, 1-hydroxyadamantane (adamantanol, see Supporting Information, supplementary Figure 1). This derivative is identical to amantadine except that instead of an amine moiety it contains a hydroxyl group.

Our electrostatic blockage hypothesis posits that adamantanol, a neutral molecule, should not be able to block the M2 channel, regardless of pH. Encouragingly, the results shown in Figure 5 are highly supportive of our hypothesis, in that adamantanol cannot block M2's channel activity even up to concentrations of 50 μM. Specifically, we observe that bacteria which express the M2 channel can barely grow in the presence of 50 μM adamantanol. In contrast, rimantadine at a much lower concentration (1.25 μM) substantially abrogates the growth retardation caused by M2 expression. Finally we note that adamantanol is not toxic to bacteria even up to concentrations of 700 μM (Supporting Information, supplementary Figure 3).

Importantly, we could prove that the lack of activity of adamantanol is solely due to the absence of a charged group, and not due to the fact that it does not bind the channel, in that both rimantadine and adamantanol bind the channel competitively. The competition is shown in Figure 5b, where we plot the growth of bacteria that express the M2 channel as a function of different rimantadine concentrations, with a resultant K_M of 13 ± 4 nM. Yet, when 50 μM adamantanol was added to the experiment (Figure 5b, red curve), the K_M of rimantadine increased to 91 ± 1 nM. The reduction of affinity of rimantadine by nearly an order of magnitude, with little or no impact on its maximal activity, due to the presence of adamantanol is a clear indication that the two drugs bind the channel competitively. In other words, adamantanol binds to the channel at the same or an overlapping binding site of rimantadine yet has no effect on the channel's conductivity.

Taken together, both the pH dependency of amantadine/rimantadine activity and the lack of activity of adamantanol provide experimental proof to our hypothesis that the source of these drugs' ability to block the channel is their charged amino group.

How M2 Mutants Develop Drug Resistance. After having established that the mechanism of inhibition of amino-adamantyls is an electrostatic repulsion of protons by their charged amino group, we turned to examine how the M2 channel develops resistance to the drugs. As stated above, we have previously shown[22] that there are two classes of mechanisms by which M2 develops resistance against amino-adamantyls: (i) mutations that result in loss of drug binding (e.g., S31N) and (ii) mutations that retain drug binding (e.g., V27A). While the mechanism of resistance of class (i) mutations is self-explanatory, the mechanism of resistance of class (ii) mutations is far less obvious. Hence, we decided to repeat the above computational analyses on the V27A mutant in hopes of gaining insight into the mechanism of drug resistance.

First, the PMF profiles for amantadine and rimantadine binding to the Singapore V27A resistant mutant were computed. As can be seen in Figure 1c, the profiles are similar to the wild-type profile (Figure 1a). The energy barriers at S22 and H37 are maintained, as well as the energy minimum at G34. However, the small barrier at V27 has been replaced with another local minimum since the physical obstruction presented by V27 was eliminated.

We next proceeded to obtain a longer trajectory of amantadine in its binding pocket for the V27A mutant. Subsequently, we analyzed the vertical movement of amantadine in the V27A channel and compared it to that in the wild-type channel. The results show that, in contrast to the relative lack of movement of the drug in the wild-type channel (Figure 2a), amantadine moves 6−7 Å from its initial position in the V27A pore, toward the N-terminus (Figure 2b). These results are consistent with the broader energy trough in the PMF profile of drug binding in the V27A mutant (Figure 1c) relative to the wild-type channel (Figure 1a).

Finally, we computed the electrostatic potential of the mutant channel, with and without amantadine bound, and compared the results to the same analysis of the wild-type channel. The results of these analyses, presented in Figure 3d−f, are most revealing.

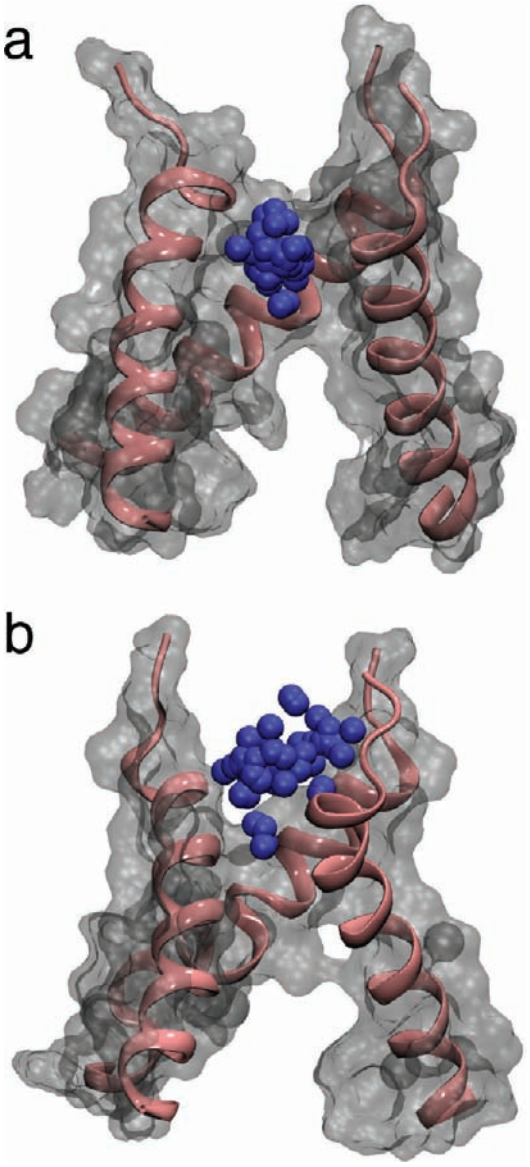

Figure 6. Snapshots of amantadine's nitrogen (blue) from unrestrained MD simulations of the channel with the positively charged inhibitor: up, wild-type channel; down, V27A channel. Only three of the helices are shown for visual clarity.

In contrast to the positive electrostatic potential induced by the charged amantadine in the wild-type channel (Figure 3b), there is no similar positive potential anywhere in the vicinity of the pore for the V27A mutant (Figure 3e)—that is to say, except for the charge originating from the H37 residues, for all states considered with and without amantadine, for both strains.

In order to understand why a charged amantadine does not result in a positive electrostatic potential in the V27A mutant, we decided to monitor its position as a function of time and compare the results with those obtained with the wild-type channel. Despite the relative stability of amantadine's center of mass in the channel upon convergence, as exhibited in Figure 2, the amine group of the molecule moves by a larger extent when bound to the V27A mutant. In the wild-type structure, amantadine's movement is restricted by V27 from above and repelled by H37 from below. Therefore, amantadine's movement is limited, thus creating a focused positive potential in a small region, as shown in Figure 3b. However, in the V27A mutant, while the histidine repulsion remains, the valine constriction is removed (ΔV = 205.6 Å^3), so that the amine group scatters over a much larger region around the N-terminal region of the channel. This can be viewed in Figure 6, where snapshots of the amantadine's nitrogen position during the simulations are illustrated. Combining this with the PMF calculations, the PMF profile for amantadine inside the V27A channel showed a slightly shallower trough at G34, meaning that it is easier for amantadine to escape from its local minimum, thereby resulting in charge delocalization.

CONCLUSION

The results presented in this work point to a self-consistent picture detailing the mechanism of inhibition of amino-adamantyls. The charged amino group produced a positive electrostatic potential in the channel lumen that results in an electrostatic repulsion of protons. This mechanism is similar to that used by aquaporin to prevent proton flux through the channel,[40−44] whereby a positive electrostatic field in the region of the NPA motif is thought to serve as the major discriminating determinant for protons and other positive charges. It is also interesting to speculate whether the electrostatic blocking mechanism might be a more general phenomenon, considering the fact that many blockers of cation channels are positively charged, while blockers of anion channels are negatively charged. This speculation must take into account the fact that any channel is designed such that it attracts a solute of a given charge, and therefore it is of no surprise that the solute and the blocker share the same charge.

Finally, we provide a molecular explanation for how a channel can develop resistance to a particular blocker, despite the fact that its retains drug binding. In the model shown schematically in Figure 7, three separate scenarios are shown. The wild-type channel has a binding pocket delimited by V27 and S31 that is appropriately sized to fit amantadine snugly (Figure 7a). Hence, the bound drug remains relatively immobile, and its charged amine can exert a positive potential that will repel and prevent any proton from traversing the pore. Resistant mutants employ two distinct strategies to avoid channel blockage. In the obvious route, mutations to larger resides at position 31 (e.g., S31N) occlude the binding site, and therefore the drug cannot bind and inhibit activity (Figure 7c). In contrast, mutations to smaller residues at position 27 (e.g., V27A) result in an increase in the binding pocket volume of 205 Å^3 (Figure 7b). This volume increase is larger than the volume of amantadine. Therefore, upon binding to the channel, the drugs remain sufficiently mobile and cannot exert a positive potential to hinder proton movement. Taken together, these detailed insights into the mechanism of drug resistivity may aid in designing new inhibitors against the virus.

MATERIALS AND METHODS

Simulation Setup. The structures used in this study were derived from the X-ray structure of the M2 channel, solved in octyl-β-D-glucopyranoside micelles, at pH 7.3, PDB code 3BKD.[28] The protein was embedded in a pre-equilibrated dimyristoylphosphocholine (DMPC) hydrated bilayer. Lipids that collided with the protein in the range of 1 Å were automatically removed. A visual inspection followed in order to manually remove further clashes that existed. Crystal waters, represented as oxygens atoms in the original PDB structure, were kept, and hydrogen atoms were added to them so that whole water molecules

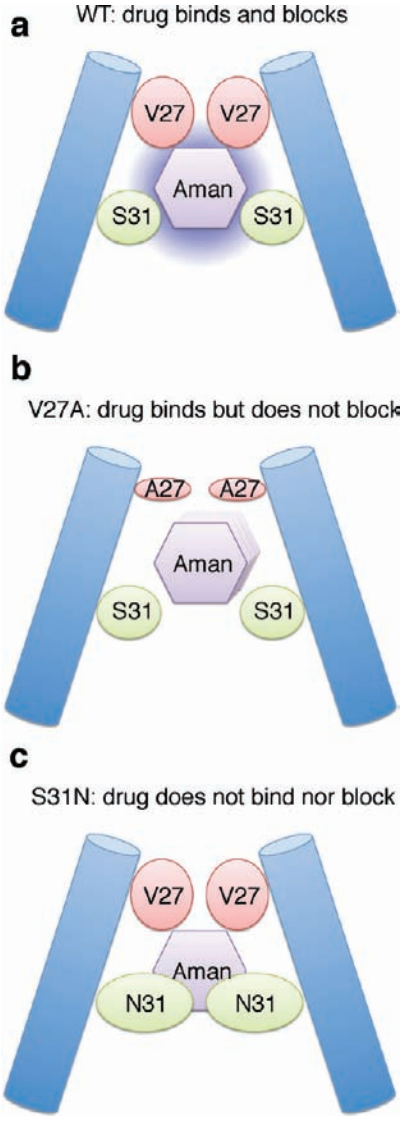

Figure 7. Resistance mechanism of M2 toward amino-adamantyls. Two out of the four helices of M2 are shown for clarity. The binding site for the amino-adamantyls is between residues 27 (red) and 31 (green), as shown in the X-ray structure.[28] In the wild-type channel (a), the drug (labeled as Aman) fits well in its binding pocket, but in the V27A mutant (b), the binding pocket has enlarged and the drug is free to move about. In the S31N mutant (c), a separate resistance mechanism in shown whereby the binding pocket has decreased such that the drug can no longer bind. A blue halo around amantadine indicates the positive electrostatic potential that is formed due to the drug.

were simulated. The residues of selenomethionine in position 33 of each helix in the original structure were mutated back to isoleucine, to correspond to the Singapore wild-type strain of M2. The N-terminus was acetylated, and the C-terminus was methyl-amidated.

Since no X-ray structures of amantadine-resistant mutants exist, a modified version of the wild-type protein was used in order to simulate amantadine-resistant mutants. The wild-type protein was mutated *in silico* using the program Swiss-PdbViewer.[45] The overall system's charge was neutralized by adding one Na^+ ion.

System Equilibration. Each system was subjected to energy minimization with the conjugate gradient algorithm and a tolerance of 200 kJ mol^{-1} nm^{-1}, followed by a minimization with the BFGS algorithm and a tolerance of 100 kJ mol^{-1} nm^{-1}.

A gradual positional restraints procedure was used to prevent high perturbations at the beginning of the simulation. This procedure is described in detail elsewhere,[46,47] except that we used a step size of dk =10 from K = 1000 to 70 kJ mol^{-1} nm^{-2}, followed by a step size of dk =1 from K = 69 to 0 kJ mol^{-1} nm^{-2}. All systems were equilibrated using MD simulations for 20 ns, and a representative structure was chosen from the most significant cluster of each simulation.

MD Simulation Parameters. The simulations were conducted using version 3.3.1 of the GROMACS simulation package[48] employing the united atoms GROMOS96 53a6 force field.[49] The DMPC force-field parameters were taken from Berger and co-workers.[50] The LINCS algorithm[51] was used to constrain bond lengths and angles of hydrogen atoms, allowing for an integration time step of 2 fs. Atomic coordinates were saved every 10 ps. The simulations were performed at a constant temperature of 310 K. Solvent, lipids, and protein were each coupled separately to a Nosé−Hoover temperature bath,[52,53] with a coupling constant of τ = 3 ps. The pressure was kept constant by a semi-isotropic, Parrinello−Rahman pressure coupling[54,55] of 1 bar, with a coupling constant of τ = 1 ps. A cutoff of 1.2 nm was used for van der Waals interactions. Electrostatic interactions were computed using the PME algorithm,[56] with a 1.2 nm cutoff for the direct space calculation. The simulations contain ∼100 DMPC lipids and ∼3600 water molecules in the FLEXSPC model.[57,58] The total number of atoms was ∼16 500.

Potential of Mean Force. The free energy of amantadine and rimantadine along the M2 pore axis (aligned to the z-axis) was calculated in the form of 1D-PMF using umbrella sampling.[59] The topology of each inhibitor was obtained from the Dundee PRODRG 2.5 server using the full-charges topology.[60] The inhibitor's center of mass was restrained with a harmonic potential to positions along the z-axis, with a force constant of 10 kcal mol^{-1} nm^{-2}. The inhibitor was placed at 69 independent z positions (windows), separated by Δz = 1 Å, thereby traversing the entire range of pore, the lipid head-groups, and the water on each side of the bilayer. In earlier simulations and docking of the inhibitors to the triprotonated channel (data not shown), we have observed the inhibitor flip so that its positively charged amine group is favored when facing the N-terminal side of the pore and opposite from the charged histidines. Thus, this was the orientation we employed for the PMF calculations.

Each window was independently subjected to an energy minimization with the BFGS algorithm with a tolerance of 100 kJ mol^{-1} nm^{-1} while the inhibitor was restrained to the z-axis only, moving freely in the xy plane in order to maintain its position along the reaction coordinate. Energy minimization was followed by a position-restrained MD of 1 ns, where the inhibitor was fixed in all dimensions while the bilayer and the protein were free to adjust around it. Each window was then simulated with the umbrella potential for 1 ns.

The biased distributions of the inhibitor's center of mass on the z-axis were examined to ensure an overlap between each window and its two adjacent windows. WHAM was used with 300 bins and a tolerance of 10^{-3} to unbias the umbrella potential and construct the energy profiles.[34] In addition, the distribution of the amino acids' positions along the pore was calculated and fitted to the PMF profile.

Unrestrained MD of Amantadine inside M2. The position of amantadine on the z-axis which yielded the lowest free energy was then used in further unrestricted MD simulations of 20 ns with the same parameters as described above. A similar simulation was performed with a neutral amantadine. The position of amantadine was recorded from the trajectory, and its movement along the z-axis was examined to see how far amantadine moved from its original position and how much it moved overall. Furthermore, a calculation of an ensemble-averaged electrostatics was performed with the PME electrostatics module in VMD,[61,62] thereby generating a smoothed electrostatic potential grid for each simulation. For comparison, the PME calculations were made for the wild-type channel and for the V27A mutant, with and without

amantadine, where amantadine was again simulated in both its charged and neutral states. The simulation of the neutral state of amantadine in M2 was tested in only one trial, whereas the rest of the simulations were performed with three trials for each configuration.

Analysis. All simulations were visualized with the Visual Molecular Dynamics (VMD) program.[62] The protocols of the simulations and the various analyzes were made using VMD, the GROMACS analysis package, and in-house Perl and Tcl scripts.

Chemicals. Amantadine, rimantadine, and 1-hydroxyadamantane (adamantanol) were purchased from Sigma-Aldrich (St. Louis, MO), while isopropyl-β-D-thiogalactopyranoside (IPTG) was purchased from Biochemika-Fluka (Buchs, Switzerland). The pMal-p2x vector was purchased from New England Biolabs (Ipswich, MA). Tuner (DE3) and DH10B bacteria were purchased from Novagen (Gibbstown, NJ) and Invitrogen (Carlsbad, CA), respectively.

Plasmids and Bacterial Strains Design. The Singapore M2 wild-type construct was designed according to the Singapore H2N2 isolate, M2 sequence.[18] The gene was flanked by the *Nco*I and *Hin*dIII restriction sites in the pUC57 plasmid. The sequence was transferred with the former two restriction sites into the pMal-p2x plasmid via the *Xmn*I and *Xba*I restriction sites, in frame to the carboxy terminus of the MalE protein, following a poly-Asn site. Growth was conducted with the DH10B or Tuner (DE3) cells.

Cells Growth. Cells bearing or lacking (as a reference) the ion channel genes were incubated overnight in LB medium containing 100 μg/mL ampicillin. Thereafter, the culture was diluted 100-fold. Next, 0.1% glucose was added, and the bacteria were grown until their OD600 reached 0.07−0.1, after which IPTG (60 μM final concentration) was added to the growth culture. Cells were then divided into 96-well flat-bottom plates containing the different treatments (growth volume of 100 μL). The plates were incubated for 16 h at 30 °C in a Synergy 2 multidetection microplate reader from Biotek (Winooski, VT) at a constant high shaking rate. OD600 readings were recorded every 15 min.

Inhibitory Constant Derivation. Monod coefficients (K_s) were derived by measuring the dose−response effect of rimantadine upon the maximal growth rate of the host bacteria. The maximal growth rates were obtained from the peaks in the graph indicating the change of the OD600 as a function of time. The resulting data were nonlinearly fitted according to the Monod equation relating the growth rate (R) to the drug concentration:

$$R = \frac{R_{max}[\text{drug}]}{K_s + [\text{drug}]}$$

Note that the control data (i.e., data without any drug) were subtracted from the results in order to serve as a reference.

pH Experiments. Bacteria were grown as above in a pH range of 5.5−9 (ΔpH = 0.5), whereby the buffering was done with 10 mM Bis-tris propane. The IPTG concentration was 40 μM, and the growth temperature was 28 °C. To each of the different bacterial cultures, 100 μM amantadine or rimantadine was added, and the effect upon growth was compared to similar cultures without addition of the drug. The percentages of inhibition or rescue were calculated by comparing the overnight OD600 of cultures relative to an untreated culture.

■ ASSOCIATED CONTENT

Supporting Information. Three additional figures. This material is available free of charge via the Internet at http://pubs.acs.org.

■ AUTHOR INFORMATION

Corresponding Author
arkin@huji.ac.il

Present Addresses
‡ Department of Theoretical and Computational Biophysics, Max Planck Institute for Biophysical Chemistry, Am Fassberg 11, D-37077 Göttingen, Germany

Author Contributions
† These authors contributed equally to this work

■ ACKNOWLEDGMENT

This work was supported in part by grants from the Israeli Science Foundation (784/01, 1249/05, and 1581/08 to I.T.A.). I.T.A is the Arthur Lejwa Professor of Structural Biochemistry at the Hebrew University of Jerusalem.

■ REFERENCES

(1) Pinto, L. H.; Holsinger, L. J.; Lamb, R. A. *Cell* **1992**, *69*, 517–528.
(2) Sakaguchi, T.; Tu, Q.; Pinto, L. H.; Lamb, R. A. *Proc. Natl. Acad. Sci. U.S.A.* **1997**, *94*, 5000–5005.
(3) Mercer, J.; Schelhaas, M.; Helenius, A. *Annu. Rev. Biochem.* **2010**, *79*, 803–833.
(4) Wang, C.; Lamb, R. A.; Pinto, L. H. *Biophys. J.* **1995**, *69*, 1363–1371.
(5) Duff, K. C.; Kelly, S. M.; Price, N. C.; Bradshaw, J. P. *FEBS Lett.* **1992**, *311*, 256–258.
(6) Kukol, A.; Adams, P. D.; Rice, L. M.; Brunger, A. T.; Arkin, I. T. *J. Mol. Biol.* **1999**, *286*, 951–962.
(7) Torres, J.; Arkin, I. T. *Biophys. J.* **2002**, *82*, 1068–1075.
(8) Torres, J.; Kukol, A.; Goldman, J.; Arkin, I. T. *Biopolymers* **2001**, *59*, 396–401.
(9) Torres, J.; Kukol, A.; Arkin, I. T. *Biophys. J.* **2000**, *79*, 3139–3143.
(10) Torres, J.; Adams, P. D.; Arkin, I. T. *J. Mol. Biol.* **2000**, *300*, 677–685.
(11) Lin, T. I.; Schroeder, C. *J. Virol.* **2001**, *75*, 3647–3656.
(12) Vijayvergiya, V.; Wilson, R.; Chorak, A.; Gao, P. F.; Cross, T. A.; Busath, D. D. *Biophys. J.* **2004**, *87*, 1697–1704.
(13) Kass, I.; Arkin, I. T. *Structure* **2005**, *13*, 1789–1798.
(14) Chen, H.; Wu, Y.; Voth, G. A. *Biophys. J.* **2007**, *93*, 3470–3479.
(15) Hu, F.; Luo, W.; Hong, M. *Science* **2010**, *330*, 505–508.
(16) Sharma, M.; Yi, M.; Dong, H.; Qin, H.; Peterson, E.; Busath, D. D.; Zhou, H.-X.; Cross, T. A. *Science* **2010**, *330*, 509–512.
(17) Polishchuk, A. L.; Lear, J. D.; Ma, C.; Lamb, R. A.; Pinto, L. H.; Degrado, W. F. *Biochemistry* **2010**, *49*, 10061–10071.
(18) Hay, A. J.; Wolstenholme, A. J.; Skehel, J. J.; Smith, M. H. *EMBO J.* **1985**, *4*, 3021–3024.
(19) Hay, A. J.; Kennedy, N. C.; Skehel, J. J.; Appleyard, G. *J. Gen. Virol.* **1979**, *42*, 189–191.
(20) Bright, R. A.; Shay, D. K.; Shu, B.; Cox, N. J.; Klimov, A. I. *JAMA* **2006**, *295*, 891–894.
(21) Astrahan, P.; Arkin, I. T. *Biochim. Biophys. Acta* **2011**, *1808*, 547–553.
(22) Astrahan, P.; Kass, I.; Cooper, M. A.; Arkin, I. T. *Proteins* **2004**, *55*, 251–257.
(23) Sansom, M. S.; Kerr, I. D. *Protein Eng.* **1993**, *6*, 65–74.
(24) Forrest, L. R.; Kukol, A.; Arkin, I. T.; Tieleman, D. P.; Sansom, M. S. P. *Biophys. J.* **2000**, *78*, 55–69.
(25) Duff, K. C.; Gilchrist, P. J.; Saxena, A. M.; Bradshaw, J. P. *Virology* **1994**, *202*, 287–293.
(26) Hu, J.; Asbury, T.; Achuthan, S.; Li, C.; Bertram, R.; Quine, J. R.; Fu, R.; Cross, T. A. *Biophys. J.* **2007**, *92*, 4335–4343.
(27) Yi, M.; Cross, T. A.; Zhou, H. X. *J. Phys. Chem. B* **2008**, *112*, 7977–7979.
(28) Stouffer, A. L.; Acharya, R.; Salom, D.; Levine, A. S.; Di Costanzo, L.; Soto, C. S.; Tereshko, V.; Nanda, V.; Stayrook, S.; DeGrado, W. F. *Nature* **2008**, *451*, 596–599.
(29) Schnell, J. R.; Chou, J. J. *Nature* **2008**, *451*, 591–595.

(30) Chuang, G. Y.; Kozakov, D.; Brenke, R.; Beglov, D.; Guarnieri, F.; Vajda, S. *Biophys. J.* **2009**, *97*, 2846–2853.
(31) Cady, S. D.; Mishanina, T. V.; Hong, M. *J. Mol. Biol.* **2009**, *385*, 1127–1141.
(32) Cady, S. D.; Schmidt-Rohr, K.; Wang, J.; Soto, C. S.; Degrado, W. F.; Hong, M. *Nature* **2010**, *463*, 689–692.
(33) Dickson, A.; Dinner, A. R. *Annu. Rev. Phys. Chem.* **2010**, *61*, 441–459.
(34) Kumar, S.; Bouzida, D.; Swendsen, R.; Kollman, P.; Rosenberg, J. *J. Comput. Chem.* **1992**, *13*, 1011–1021.
(35) Hu, J.; Fu, R.; Nishimura, K.; Zhang, L.; Zhou, H. X.; Busath, D. D.; Vijayvergiya, V.; Cross, T. A. *Proc. Natl. Acad. Sci. U.S.A.* **2006**, *103*, 6865–6870.
(36) Astrahan, P.; Flitman-Tene, R.; Bennett, E. R.; Krugliak, M.; Gilon, C.; Arkin, I. T. *Biochim. Biophys. Acta* **2011**, *1808*, 394–398.
(37) Spector, R. *J. Pharmacol. Exp. Ther.* **1988**, *244*, 516–519.
(38) Bleidner, W. E.; Harmon, J. B.; Hewes, W. E.; Lynes, T. E.; Hermann, E. C. *J. Pharmacol. Exp. Ther.* **1965**, *150*, 484–490.
(39) Holazo, A. A.; Choma, N.; Brown, S. Y.; Lee, L. F.; Wills, R. J. *Antimicrob. Agents Chemother.* **1989**, *33*, 820–823.
(40) de Groot, B. L.; Grubmüller, H. *Science* **2001**, *294*, 2353–2357.
(41) de Groot, B. L.; Frigato, T.; Helms, V.; Grubmüller, H. *J. Mol. Biol.* **2003**, *333*, 279–293.
(42) Chakrabarti, N.; Roux, B.; Pomès, R. *J. Mol. Biol.* **2004**, *343*, 493–510.
(43) Ilan, B.; Tajkhorshid, E.; Schulten, K.; Voth, G. A. *Proteins* **2004**, *55*, 223–228.
(44) Kato, M.; Pisliakov, A. V.; Warshel, A. *Proteins* **2006**, *64*, 829–844.
(45) Guex, N.; Peitsch, M. C. *Electrophoresis* **1997**, *18*, 2714–2723.
(46) Leonov, H.; Arkin, I. T. *Eur. Biophys J.* **2010**, *39*, 1043–1049.
(47) Leonov, H.; Arkin, I. T. *J. Mol. Model.* **2009**, *15*, 1317–1328.
(48) Lindahl, E.; Hess, B.; van der Spoel, D. *J. Mol. Model.* **2001**, *7*, 306–317.
(49) Oostenbrink, C.; Villa, A.; Mark, A. E.; van Gunsteren, W. F. *J. Comput. Chem.* **2004**, *25*, 1656–1676.
(50) Berger, O.; Edholm, O.; Jahnig, F. *Biophys. J.* **1997**, *72*, 2002–2013.
(51) Hess, B.; Bekker, H.; Berendsen, H. J. C.; Fraaije, J. G. E. M. *J. Comput. Chem.* **1997**, *18*, 1463–1472.
(52) Nosé, S. *Mol. Phys.* **1984**, *52*, 255–268.
(53) Hoover, W. G. *Phys. Rev. A* **1985**, *31*, 1695–1697.
(54) Parrinello, M.; Rahman, A. *J. Appl. Phys.* **1981**, *52*, 7182–7190.
(55) Nosé, S.; Klein, M. L. *Mol. Phys.* **1983**, *50*, 1055–1076.
(56) Darden, T.; York, D.; Pedersen, L. *J. Chem. Phys.* **1993**, *98*, 10089–10092.
(57) Berendsen, H. J. C.; Grigera, J. R.; Straatsma, T. P. *J. Phys. Chem.* **1987**, *91*, 6269–6271.
(58) *Interaction Models for Water in Relation to Protein Hydration*; Pullman, B., Ed.; D. Reidel Publishing Co.: Dordrecht, 1981.
(59) Torrie, G. M.; Valleau, J. P. *J. Comput. Phys.* **1977**, *23*, 187–199.
(60) Schuttelkopf, A. W.; van Aalten, D. M. *Acta Crystallogr. D: Biol. Crystallogr.* **2004**, *60*, 1355–1363.
(61) Aksimentiev, A.; Schulten, K. *Biophys. J.* **2005**, *88*, 3745–3761.
(62) Humphrey, W.; Dalke, A.; Schulten, K. *J. Mol. Graphics* **1996**, *14*, 33–38.